Drivers and Predictability of Summer Marine Heatwaves in the Northwest Pacific

Lifei Qiao[1,2,3], Haosu Tang[4*], Gang Huang[1,2,3*]

[1]*Key Laboratory of Earth System Numerical Modeling and Application, Institute of Atmospheric Physics, Chinese Academy of Sciences, Beijing, China*

[2]*Laboratory for Regional Oceanography and Numerical Modeling, Qingdao National Laboratory for Marine Science and Technology, Qingdao, China*

[3]*University of Chinese Academy of Sciences, Beijing, China*

[4]*School of Geography and Planning, University of Sheffield, Sheffield, UK*

* Corresponding author: haosu.tang@sheffield.ac.uk and hg@mail.iap.ac.cn

Key Points

- Dominant summer marine heatwave modes in the Northwest Pacific are obtained through MV-EOF analysis.
- The first mode corresponds to the El Niño decaying summer, while the second mode aligns with the El Niño developing summer.
- Physics-based empirical models with the leave-one-out cross-validation technique demonstrate significant predictability for these modes.

Abstract

Marine heatwaves (MHWs) in the Northwest Pacific (NWP) exert significant ecological and climatic impacts, yet their drivers and predictability are not fully understood. Based on the multivariate empirical orthogonal function (MV-EOF) method, this study identifies two dominant modes of summer NWP MHWs. The first mode, characterized by widespread warming across the low-latitude NWP, occurs during the summer following an El Niño event. This mode is strongly associated with the Pacific–Japan teleconnection pattern and sea surface temperature (SST) anomaly gradient between the North Indian Ocean and tropical western Pacific. The second mode exhibits a northeast-to-southwest tripole structure, representing the summer phase during El Niño development. This tripole pattern is possibly influenced by the North Pacific Oscillation, highlighting an extratropical–tropical teleconnection that propagates the effects of positive SST anomalies. Using physics-based empirical prediction models validated by the leave-one-out cross-validation approach, a notable degree of predictability is found for these MHW modes. The temporal correlation coefficient scores and Root Mean Square Errors between observed and predicted principal components (PC1 and PC2) reach 0.65 and 0.77 for PC1, and 0.55 and 0.84 for PC2, respectively, over the period 1982–2022. Both models effectively capture the peak intensity and spatial distribution of MHWs, despite minor discrepancies. These findings might advance our understanding of MHW dynamics in the NWP and provide a foundation for developing early warning systems to mitigate their adverse effects on marine ecosystems and coastal communities.

Plain Language Summary

Marine heatwaves (MHWs) in the Northwest Pacific (NWP) have emerged as critical climate events with profound impacts on marine ecosystems, fisheries, and regional weather patterns. However, the drivers of MHW variability are not fully understood, and predicting summer MHWs in the NWP remains a significant challenge. In this study, using the multivariate empirical orthogonal function (MV-EOF) method, we identify two dominant modes of summer MHW variability. The first mode, occurring during the summer following an El Niño event, is linked to the Pacific–Japan teleconnection pattern and Indo–Pacific sea surface temperature (SST) anomalies. The second mode, associated with the summer phase of developing El Niño events, is potentially tied to the North Pacific Oscillation. To assess the predictability of these MHW modes, we develop physics-based empirical prediction models validated through the leave-one-out cross-validation approach. The models effectively capture the peak intensity and spatial distribution of observed MHWs, demonstrating their potential for improving seasonal MHW forecasts. This study contributes to the understanding of the mechanisms driving NWP MHWs and highlights the importance of advancing predictive approaches to mitigate the ecological and socio-economic impacts of future MHW events.

1. Introduction

Marine heatwaves (MHWs) are extreme climate events characterized by prolonged periods of sea surface temperatures (SSTs) exceeding climatological thresholds (Hobday et al., 2016). Since the early 20th century, the intensity, duration, frequency, and total occurrence of MHWs have significantly increased due to rising background SSTs (Frolicher et al., 2018). While MHWs have garnered less attention compared to terrestrial heatwaves, they pose a serious threat to ocean ecosystems, potentially reshaping marine habitats and disrupting ecological services (Wernberg et al., 2013). These disruptions can lead to substantial declines in marine biodiversity and productivity (Smale et al., 2019). Several notable MHWs, including the Northwest Atlantic MHW in 2012 (Mills et al., 2013), the Tasman Sea MHW in 2015/16 (Oliver et al., 2017), and the North Pacific MHW in 2014/15 (Di et al., 2016), have led to serious impacts on marine ecosystems and coastal economies. Projections suggest that large portions of the global ocean could experience near-permanent MHW conditions by the end of the 21st century (Oliver et al., 2019). Therefore, improving the understanding and prediction of MHWs is crucial for enhancing marine ecosystem resilience and mitigating their economic and societal consequences.

Accurate prediction of MHWs relies on understanding their underlying physical drivers. Recent studies have revealed that MHWs are closely linked to key atmospheric and oceanic processes, including increased solar radiation, reduced oceanic heat loss, and a shallower mixed layer (Yao et al., 2023; Lyu et al., 2024). For instance, MHWs in the South China Sea (SCS) are significantly influenced by the position and magnitude of West Pacific subtropical high (WPSH) (Song et al., 2023). This high-pressure system reduces cloud cover and weakens wind speed by suppressing local convection over the Northwest Pacific (NWP), resulting in enhanced downward shortwave radiation and reduced latent heat loss. Additionally, SCS MHWs exhibit a distinct life cycle associated with El Niño–Southern Oscillation (ENSO) during 1982–2018. Based on ENSO-related SSTA, Liu et al. (2022) classified SCS MHWs into three categories: El Niño-P1, corresponding to the initial warming peak of El Niño; El Niño-P2, occurring during the secondary warming peak; and La Niña-P1, characterized by a single warming peak during La Niña. All three types are modulated by an intensified lower-level anticyclone over the NWP. The first empirical orthogonal function (EOF) mode further reveals a dominant single-signal pattern across the entire SCS (Yao et al., 2021). Moreover, MHWs in the East China Sea and South Yellow Sea during boreal summers from 2016 to 2018 were strongly influenced by the East Asian summer monsoon, driven by interactions between the WPSH and the mid-level westerly jet, with shortwave radiation and oceanic advection anomalies playing key roles (Gao et al., 2020). For the broader NWP, which supports vital fisheries and aquaculture industries essential to the economy and food security of surrounding countries, a comprehensive understanding of MHWs is crucial. Notably, Hokkaido’s fisheries, situated at the confluence of the Kuroshio and Oyashio currents, serve as a central hub for North Pacific fisheries. Commercial species such as scallops, chum salmon, and various shellfish, along with aquaculture operations for seaweed, oysters, and prawns, are highly vulnerable to MHWs. Given the potential of these extreme events to disrupt marine industries, advancing our understanding of NWP MHWs is essential for mitigating socio-economic losses, enhancing marine ecosystem resilience, and safeguarding the livelihoods of coastal communities.

At present, MHW predictions primarily focus on seasonal forecasts. Jacox et al. (2022) employed a large ensemble of global climate model forecasts to predict MHWs up to twelve months in advance, depending on the region, season, and prevailing large-scale climate modes. Similarly, hindcasts from the coupled climate forecast system (version 1.0) of the Nanjing University of Information Science and Technology (NUIST-CFS1.0) have demonstrated skill in forecasting the spatial distribution of total

MHW days over the NWP during summer with a lead time of up to eight months, as well as capturing the linear trend and interannual variability at lead times of up to nine and three months, respectively (Zhang et al., 2023). The predictive skill for MHWs in the NWP also exhibits notable seasonal dependence, with higher skill observed from mid-summer to early autumn, when ENSO serves as a key source of predictability (Ma et al., 2024). In recent years, machine learning (ML) techniques have gained attention in ocean forecasting, with methods such as random forests, long short-term memory networks, and convolutional neural networks being used to develop predictive models for SST (Bonino et al., 2023). However, ML techniques are sometimes criticized for their lack of interpretability in terms of physical processes (Zhang et al., 2022), raising concerns about their reliability and accuracy in real-world scenarios (de Burgh-Day et al., 2023). The black-box nature of many ML models implies that while they may yield statistically accurate predictions, they may fail to fully capture the complexities of underlying physical mechanisms. Therefore, this study aims to identify effective precursor factors combined with physical mechanisms and establish physics-based empirical models that integrate dynamical processes with statistical methods (Li et al., 2016; Long et al., 2022; Yao et al., 2024). Rather than simply forecasting the magnitude of regional-mean MHWs, this approach seeks to provide a framework for predicting the spatial patterns of NWP MHWs, ensuring more reliable and physically grounded predictions.

Previous studies have demonstrated that summer atmospheric circulation and SST anomalies in the NWP are closely linked to ENSO events in the preceding winter. During the El Niño decaying spring, an equatorial asymmetric mode of rainfall and surface wind patterns emerges over the tropical Indian Ocean (TIO) (Wu et al., 2008). This antisymmetric atmospheric pattern persists through the positive wind–evaporation–SST (WES) feedback until the El Niño decaying summer, further inducing TIO basin warming. The TIO warming triggers a Matsuno–Gill response in the troposphere (Matsuno, 1966; Gill, 1980), leading to the formation of anomalous anticyclonic circulation (AAC) and positive SST anomalies in the low-latitude NWP through low-level Ekman divergence (Xie et al., 2009). The easterly wind anomalies on the southern periphery of the AAC further reinforce TIO warming by weakening the westerly monsoon winds (Kosaka et al., 2013), while simultaneously promoting NWP cooling by intensifying the easterly trade winds. This cross-basin positive feedback between the AAC and SST anomalies amplifies the influence of ENSO on the Indo–NWP climate during the summer following El Niño.

While SST anomalies in the NWP are influenced by preceding ENSO events, the relationships between local MHWs and broader tropical and extratropical climate modes remain insufficiently explored. Moreover, the extent to which the NWP MHW variability can be predicted requires further exploration. This study aims to address the following key questions: (1) What are the leading modes of the NWP MHW variability? (2) What are the dynamic origins of these modes? (3) What are the physically significant precursors of these modes, and can the physics-based empirical model effectively predict them? The remainder of this paper is organized as follows: Section 2 describes the data and methods used in this study. Section 3 examines the spatial and temporal characteristics of NWP MHWs and explores the physical mechanisms driving their dominant modes. In Section 4, we develop a set of physics-based empirical models to predict the spatial patterns of NWP MHWs. Finally, Section 5 presents the conclusions and discussion.

2. Data and methods

2.1 Datasets

In this study, we analyze the characteristics of boreal summer (June–August, JJA)

NWP MHWs over a 41-year period from 1982 to 2022. The global precipitation data used in this study are sourced from the Climate Prediction Center (CPC) Merged Analysis of Precipitation (CMAP) (Xie et al., 1997), which provides monthly averages at a 2.5°×2.5° resolution, available since January 1979. Monthly mean horizontal wind data are from the fifth-generation European Centre for Medium-Range Weather Forecasts (ECMWF) reanalysis (ERA5) (Hersbach et al. 2023), with 37 vertical levels ranging from 1000 hPa to 1 hPa and a horizontal resolution of 0.25°×0.25°. Monthly SST data are obtained from the Hadley Centre Sea Ice and SST dataset (HadISST) dataset (Rayner et al., 2003), which provides SST measurements at a 1°×1° resolution from 1870 onwards. The observed daily SST data are acquired from the National Oceanic and Atmospheric Administration (NOAA) Optimum Interpolation SST version 2 (OISST v2) High-Resolution dataset, with a spatial resolution of 0.25° × 0.25°, covering the period from 1982 to 2022 (Huang et al., 2021).

Phytoplankton chlorophyll-a concentration, a key indicator of primary productivity and phytoplankton biomass in marine environments, is strongly influenced by SST variations. In this study, monthly chlorophyll-a concentration data are obtained from the Aqua Moderate Resolution Imaging Spectroradiometer (MODIS) with a spatial resolution of 9km × 9km and a time span of 2003–2022 (NASA Goddard Space Flight Center, O. B. P. G., 2018).

To explore the underlying physical drivers of MHWs, we examine simultaneous changes in key atmospheric and oceanic variables, including horizontal winds, surface heat fluxes, ocean currents, and ocean temperature. Monthly mean surface heat flux components are obtained from the National Centers for Environmental Prediction–Department of Energy (NCEP–DOE) Reanalysis II dataset (Kanamitsu et al. 2002), including Upward Longwave Radiation Flux (ULRF), Downward Longwave Radiation Flux (DLRF), Upward Shortwave Radiation Flux (USRF), Downward Shortwave

Radiation Flux (DSRF), Sensible Heat Flux (SHF), and Latent Heat Flux (LHF). These surface flux datasets are available from January 1979 onward at a spatial resolution of 2.5° × 2.5°. The monthly zonal (u) and meridional (v) components of ocean currents are sourced from the NCEP Global Ocean Data Assimilation System (GODAS), available from January 1980 onward (Behringer et al., 1998). Ocean temperature data are retrieved from the EN4 dataset (Good et al., 2013), which provides temperature profiles at a 1° × 1° resolution from 1900 onward. For consistency, all datasets have been interpolated onto a uniform 1° × 1° horizontal grid before formal analysis.

2.2 Methods

In this study, MHWs are identified when SSTs exceed the 90th percentile threshold of a 30-year historical reference period (1983–2012) for at least five consecutive days, based on a 5-day running mean (Hobday et al., 2016). MHW events separated by two days or less are considered a single continuous event. The daily intensity of MHWs at each grid point is defined as the difference between the observed SST and the threshold during MHW events, with values set to 0.0 outside these periods. To provide a more comprehensive assessment of MHW characteristics, we employ the cumulative magnitude index (CMI), which integrates intensity, duration, and frequency to quantify MHW properties (e.g., Hu et al., 2020). This index allows for comparative analyses of MHW events across different regional scales, and is defined as follows:

$$CMI = \sum_{i=1}^{n} \sum_{d=1}^{d_i} T_{(i,d)} \tag{1}$$

where n represents the frequency of MHWs during the research period, d_i denotes the duration of the ith MHW event, and $T_{(i,d)}$ indicates the daily intensity of the MHW on day d of the ith event.

To capture the coherent spatiotemporal characteristics of NWP MHWs, we apply multivariate EOF (MV-EOF) analysis to the CMI and 850 hPa zonal winds from 1982 to 2022 (Wang, 1992). This method provides insights into the dominant spatial and temporal patterns of MHW variability across the region and facilitates the further construction of the prediction model. The North significance test is used to assess whether the leading eigenvalues are significantly distinguishable. For validation, traditional EOF analysis on the CMI is performed as well, yielding similar results. Additionally, we employ the upper-ocean mixed layer heat budget equation to diagnose the drivers behind the leading modes of MHWs. The mixed layer heat budget is calculated according to the following equation:

$$\Delta T = \frac{Q'_{net}}{\rho c_p H} + D + R \tag{2}$$

where T is the mixed layer potential temperature; ρ $(= 10^3 kg\ m^{-3})$ is the density of ocean water; C_p $(= 4000\ J\ kg^{-1}\ K^{-1})$ is the specific heat capacity of water; H is the climatological mixed layer depth as a constant 50m; D denotes the oceanic dynamic processes. It is defined as $D = \langle -u' \frac{\partial \bar{T}}{\partial x} \rangle + \langle -\bar{u} \frac{\partial T'}{\partial x} \rangle + \langle -u' \frac{\partial T'}{\partial x} \rangle + \langle -v' \frac{\partial \bar{T}}{\partial y} \rangle + \langle -\bar{v} \frac{\partial T'}{\partial y} \rangle + \langle -v' \frac{\partial T'}{\partial y} \rangle + \langle -w' \frac{\partial \bar{T}}{\partial z} \rangle + \langle -\bar{w} \frac{\partial T'}{\partial z} \rangle + \langle -w' \frac{\partial T'}{\partial z} \rangle$, where $u, v,$ and w denote three-dimensional components of ocean current velocity. Here, the overbars represent the climatological mean, and the primes refer to the regression anomalies. R represents the residual term. Q_{net} is defined as $Q_{net} = Q_{SRF} + Q_{LRF} - Q_{LHF} - Q_{SHF}$, indicating net sea surface heat flux processes. Q_{SRF} and Q_{LRF} represent net shortwave radiation (DSRF minus USRF) and net longwave radiation (DLRF minus ULRF), respectively (downward positive). Q_{LHF} and Q_{SHF} denote LHF and SHF, respectively (upward positive). Given the typically small contribution of nonlinear advection terms and the lack of vertical current velocity data, this study focuses on oceanic thermodynamic terms and dynamic terms associated with horizontal currents to investigate the underlying physical mechanisms.

To further assess the impact of the SST anomaly gradient between El Niño-induced North Indian Ocean (NIO) warming and tropical western Pacific (WP) cooling on atmospheric responses over the NWP, we use the atmospheric component of the MPI-ESM, ECHAM6. It is a general circulation model with a spectral resolution of T63 (corresponding to a 92 × 196 grid in latitude and longitude) and 47 vertical levels. The first experiment, termed the Control run, is driven by global climatological SST and sea ice with a seasonal cycle. Following this, three sensitivity experiments are conducted to investigate regional SST anomaly impacts. In the NIO run, a +1°C SST anomaly is applied in the NIO (0°–25°N, 40°E–100°E) and added to the climatological SST as the boundary condition. The WP run follows a similar approach, imposing a -1°C SST anomaly in the WP (5°S–5°N, 160°E–150°W). The NIO–WP run combines these configurations, applying a +1°C SST anomaly in the NIO and a -1°C SST anomaly in the WP. Details of the SST boundary conditions for each experiment are provided in Table 1. Each experiment is integrated over a 40-year period, with the climatological SST forcing repeated annually. To reduce the effects of internal variability, results from the last 30 ensemble members are averaged.

The physics-based empirical model is a prediction method grounded in the understanding of physical mechanisms. Different from purely statistical approaches, it employs only predictors with a direct physical linkage to the predictand (Long et al., 2022). This approach not only predicts time series but also captures spatial patterns. Specifically, the first step involves selecting potential predictors through lead-lag regression analysis between the principal components (PCs) and anomalies in lower boundary conditions. The second step assumes that these potential predictors hold physical significance. Predictors are defined over a broad range where the correlation coefficient is significant at the 99% confidence level, as follows:

$$Pred(t) = [VAL(t, lat, lon) \times TCC(lat, lon)] \quad (3)$$

where VAL denotes potential predictors at lead time t for each grid point, while TCC refers to the temporal correlation coefficient between the predictand and corresponding VAL values at each gird during the training period. The square bracket indicates the area-weighted regional mean over the selected regions.

Following the aforementioned steps, we use the stepwise regression to identify key predictors and ensure their mutual independence in constructing physics-based empirical models. To evaluate the performance of the regression model and minimize overfitting, we implement the leave-one-out cross-validation technique. In this study, the JJA CMI for each year is predicted using data from the remaining years. The process involves two steps: (a) setting aside one year as the test dataset while developing a regression model using the remaining $n-1$ observations, and (b) applying this model to predict the PCs for the excluded year, yielding a series of predicted values. We remove the linear trends from datasets before formal analyses to exclude the impact of global warming, and use the two-tailed Student's *t*-test to evaluate the significance of regression and correlation analyses.

2.3 Study region

The NWP encompasses the Indo–Pacific Warm Pool, the largest warm water region on the planet. This area is characterized by consistently high SSTs, often exceeding 28°C, and substantial precipitation during the boreal summer months (Figure 1a). Strategically located at the intersection of easterly and westerly wind systems, the low-latitude NWP is influenced by various weather and climate systems, including typhoons, monsoons, mesoscale eddies, and ENSO. This region plays a critical role in global climate dynamics, as it hosts the upward branch of both the zonal Walker circulation and the meridional Hadley cell. With ongoing global warming, the probability density curves of SST anomalies in the NWP are shifting toward higher levels (Figure 1b). As SSTs increase, local regions experience warmer background conditions, potentially leading to a higher frequency of MHW occurrences.

3. Leading modes of NWP MHWs and associated mechanisms

Figure 1c illustrates the climatological spatial distribution of CMI in the NWP during summer from 1982 to 2022. The CMI exceeds 3°C across most of the NWP, particularly in regions influenced by the western boundary current. The most prominent hotspot for NWP MHWs is the Kuroshio–Oyashio extension, located east of Japan. Over the period from 1982 to 2022, the CMI has increased across nearly the entire NWP (Figure 1d), with a regional mean trend of 2.2°C per decade ($p < 0.01$). This increase is especially pronounced in mid-latitude areas influenced by the Japanese warm current. Sub-seasonal variations of the area-weighted regional mean CMI during summer are depicted in Figure 1e. A marked rise in CMI is evident after 1998, with severe NWP MHW events occurring in July–August 1998, June–July 2001 and 2010, and each summer from 2014 to 2022. Notably, since the late 1990s, the regions influenced by severe MHWs have expanded from limited oceanic areas (~ 30°N–40°N) to encompass the entire mid- to low-latitude range (Figure 1f).

To identify the dominant modes of MHW variability in the NWP over the past 41 years, we conduct MV-EOF analysis on CMI and 850hPa zonal winds from 1982 to 2022. Given the relatively low contributions of the higher-order modes, we focus on the leading two MV-EOF modes, which are significantly separated according to North's significance test. A traditional EOF analysis on CMI yields similar spatial patterns, with correlation coefficients of 0.83 and 0.70 for PC1 and PC2, respectively, when compared to the MV-EOF results (Figure S1). Figure 2 demonstrates the spatial and temporal characteristics of these modes. The first MV-EOF mode, accounting for 21.49% of the total variance, exhibits a robust basin-wide warming from the equator to 30°N, with the most pronounced signal in the SCS (Figure 2a). This mode is associated with a strong lower-level AAC, reminiscent of the tropical segment of the Pacific–Japan (PJ) teleconnection pattern (Figure S2). The corresponding PC (PC1) shows pronounced interannual variability, with peaks in 1983, 1988, 1995, 1998, 2010, 2020, and 2022 (Figure 2b). Moreover, an inter-decadal variation is observed in PC1 as well, with more intense anomalies occurring since the late 1990s. The positive phase of this mode is linked to reduced chlorophyll-a concentrations in the lower latitudes of the NWP (Figure 3a). The overall negative correlation between CMI and chlorophyll-a indicates that local MHWs may suppress phytoplankton biomass and productivity, possibly through increasing ocean stratification and shoaling the mixed layer depth (Chen et al., 2023; Zheng et al., 2024).

The second MV-EOF mode exhibits a tripole pattern, characterized by a warm-cold-warm distribution extending from the northeast to the southwest. In this pattern, cold-surge zones are identified in the eastern low-latitude Mariana Basin and the East China Sea, coinciding with the southern and western flanks of the AAC, respectively (Figure 2c). This mode accounts for 11.75% of the total variance, with the corresponding PC (PC2) displaying pronounced interannual variability, marked by notable events in the summers of 1982, 1987, 1992, 1993, 2002, and 2015 (Figure 2d). In general, cold-surge zones are associated with anomalously high chlorophyll-a concentrations, whereas regions with elevated CMI tend to exhibit lower chlorophyll-a levels (Figure 3b).

To investigate the underlying mechanisms driving the leading two dominant modes, regressions of SRF, LRF, SHF, and LHF anomalies against each PC from 1982 to 2022 are shown (Figure 4). In the basin-wide mode, SRF and LHF anomalies emerge as the primary contributors to surface temperature changes. In contrast, LRF anomalies play a relatively minor role, while SHF anomalies are negligible (Figures 4a–d). In the low-latitude NWP, the presence of a lower-level AAC induces anomalous descending airflow, which reduces cloud cover and allows more SRF to reach the ocean surface, thereby increasing local CMI (Figure 4a). Besides, easterly anomalies along the southern flank of AAC weaken the prevailing westerly winds over the low-latitude NWP. This weakening reduces LHF loss from the ocean, facilitating heat retention within the mixed layer, ultimately contributing to rising CMI and an increased likelihood of MHWs (Figure 4d).

In the tripole mode, SRF anomalies play a dominant role, whereas LHF, LRF, and SHF anomalies have comparatively minor influences. Positive SRF anomalies induced by AAC facilitate greater heat accumulation in the ocean mixed layer, fostering the development and intensification of MHWs (Figure 4e). Compared to thermodynamic processes, oceanic dynamic processes contribute less to the formation of these two MHW modes (Figure S3). Together, these findings highlight the critical role of anomalous atmospheric circulation in modulating surface fluxes, driving CMI increases, and ultimately triggering local MHWs.

4. Empirical prediction of NWP MHWs

4.1 Potential predictor identification

To capture the distinct dynamic origins of each mode and ensure the accuracy of predictability, we employ stepwise regression to identify physically relevant predictors for each PC.

To investigate the physical mechanisms through which each predictor influences the two dominant patterns, Figure 5 presents the lead-lag regression maps of the PCs against SST anomalies. The basin-wide pattern is closely linked to the summer of the

El Niño decaying phase. During the preceding December–February (DJF), the mature phase of El Niño promotes the development of NIO warming, which persists into JJA. This sustained NIO warming triggers eastward-propagating Kelvin waves, reinforcing positive SST anomalies over the NWP via AAC (Figures 5a, b). As a result, the DJF Niño3.4 index is selected as the primary predictor. Moreover, summer cooling in the WP also plays a crucial role in the development of the basin-wide pattern. Physically, cooling in the WP during summer can generate westward-propagating Rossby waves, which subsequently strengthen the AAC and enhance the CMI over the NWP (Wang et al., 2013). This summer cooling is closely linked to the decaying of El Niño, which is strongly influenced by anomalous easterlies along the southern flank of the NWP AAC in preceding seasons. Therefore, the MAM low-latitude NWP (0–15°N, 135°E–155°E) area-weighted regional mean zonal wind anomaly is selected as the second predictor, as anomalous easterlies strengthen the background northeasterly winds and accelerate El Niño's demise. To further verify the impact of SST anomaly gradient between El Niño-induced NIO warming and WP cooling on atmospheric responses over the NWP, we conduct a series of experiments using ECHAM6, which is well-suited for examining atmospheric responses to specific SST patterns. The results reveal that SST anomalies in either the NIO or WP alone can induce NWP AAC and equatorial easterly wind anomalies, but their effects are relatively weak, particularly in the subtropics (Figures 6a–d). However, when combined, the SST anomalies from both the NIO and WP produce more pronounced high-pressure anomalies across the NWP (Figures 6e–f), thereby amplifying local MHWs (Figure 5c).

In the tripole pattern, the central equatorial Pacific undergoes a gradual warming from preceding winter to summer, indicating the development of an El Niño event. This warming becomes most pronounced in the subsequent winter, when a fully developed El Niño event emerges (Figure S4). This is further supported by peak years in the PC2 time series such as 1982, 1997, and 2015, which coincide with notable El Niño developing years (Figure 2d). Accompanying El Niño development is the strong westerly wind anomalies in the equatorial Pacific, which could weaken the easterly trade winds and generate downwelling Kelvin waves. These waves propagate eastward, deepening the thermocline in the eastern Pacific, reinforcing SST warming, and further strengthening El Niño (McPhaden, 1999; Vecchi et al., 2000). Thus, the tripole pattern likely corresponds to the summer phase of El Niño development, and the MAM equatorial Pacific (5°S–5°N, 135°E–155°E) area-weighted regional mean zonal wind anomaly is selected as the first predictor of PC2.

Additionally, the North Pacific Oscillation (NPO) pattern, featuring a north–south dipole in sea level pressure (SLP) over the North Pacific, may also play a role in shaping the tripole pattern. In March, an anomalous cyclone develops over the Northeast Pacific, with its eastern flank featuring anomalous southwesterly flow that weakens the off-equatorial trade winds (Figure 7a). In the following months, the southern portion of this anomalous cyclone continues to modulate the strength of the northeasterly trade winds, leading to a warm anomaly signal in the subtropical Northeast Pacific due to changes in latent heat fluxes (Vimont et al., 2001). This signal propagates southwestward to the equatorial central Pacific from March to May via WES feedback (Figure 7), contributing to El Niño development. Meanwhile, anomalous warming in the central tropical Pacific induced by the anomalous cyclone can feedback into the North Pacific, intensifying the anomalous cyclone to its north (Ding et al., 2022). This extratropical–tropical interaction may serve as a precursor to sustain El Niño events, accompanied by the eastward extension of enhanced precipitation over the central equatorial Pacific (Figure S5). Furthermore, the westward movement of the anomalous cyclone also affects the NWP AAC near 30°N, further influencing CMI and MHWs in the NWP. Hence, the NPO index is selected as the second predictor of PC2, defined as the MAM SLP anomaly difference between the regional mean over (60°N, 140°E–170°W) and (30°N, 140°E–170°W).

In summary, the selected predictors, based on well-established physical mechanisms, exhibit significant correlations with the predictand while remaining largely independent of each other (Table S1). This supports their effectiveness in accurately predicting MHW patterns in the NWP.

4.2 Prediction skills of physics-based empirical models

Building on the physical significance of the previously identified predictors, empirical prediction models are further developed to enhance the accuracy of MHW forecasts. To evaluate predictive skill, we apply the leave-one-out cross-validation method, assessing the predicted sequences of the two modes using TCC and Root Mean Square Error (RMSE) as metrics. The predicted sequences from both modes are subsequently used to reconstruct spatial MHW patterns through regression analysis for further validation.

For PC1, the cross-validated hindcast demonstrates a TCC skill of 0.65 ($p < 0.01$) and an RMSE of 0.77 over the period from 1982 to 2022 (Figure 8a). This model successfully captures significant MHW events in most years, highlighting its strong predictive skill for the basin-wide pattern. However, it also faces limitations in accurately forecasting the strong 2020 NWP MHW, which may be due to the model's failure to account for factors like the unusually persistent Madden–Julian Oscillation (MJO) during the summer of 2020 (Zhang et al., 2021). Nonetheless, the predicted spatial patterns align well with the observed basin-wide pattern (Figure 8b), indicating that the physics-based empirical model provides a reasonably accurate representation of large-scale MHW patterns in the NWP, despite some discrepancies.

For PC2, the cross-validated hindcast achieves a TCC skill of 0.55 ($p < 0.01$) and an RMSE of 0.84 during the period from 1982 to 2022 (Figure 8c). This model performs well in predicting high-impact years linked to developing El Niño events, such as 1997 and 2015, accurately capturing the increased MHW intensity during these periods. However, while the predicted spatial patterns reflect most of the MHW regions and cold-surge areas within the tripole pattern, the model struggles with weaker MHW events in the SCS (Figure 8d). Overall, the physics-based empirical model demonstrates credible predictive capability for both PCs, though the bias is slightly larger for PC2 compared to PC1, indicating room for further refinement in prediction accuracy. Incorporating additional intra-seasonal atmospheric drivers into the model may further enhance forecast reliability and yield more accurate insights into MHW patterns in the NWP.

To further assess the prediction skills and predictability of NWP MHWs, we calculate both the reconstructed and maximum attainable TCC skill at each grid point. The reconstructed prediction field is obtained by summing the leading two predicted PCs multiplied by their corresponding observed MV-EOF modes. The maximum attainable skill is determined by calculating the TCC between the observed total field and the observed predictable modes. As shown in Figure 8, the domain-averaged reconstructed TCC skill is 0.36 (Figure 8e), approaching the ideal value of 0.50, which represents perfect prediction (Figure 8f). In addition, the high TCC skill values observed in the low-latitude NWP region (0–20°N) are likely linked to tropical ocean–atmosphere interactions. These interactions contribute to the development of tropical ocean–atmosphere modes, which provide the predictability of weather patterns and MHWs in the region.

5. Conclusions and discussion

This study investigates the drivers and predictability of summer MHWs in the NWP from 1982 to 2022. Our analysis identifies two dominant modes of NWP MHWs, namely, a basin-wide pattern strongly linked to ENSO and a northeast-to-southwest tripole structure associated with the NPO. These modes encapsulate the primary drivers of spatial variability in summer NWP MHWs, revealing critical insights into their underlying physical mechanisms.

Our results indicate the significant influence of large-scale atmospheric circulation on the variability of NWP MHWs, supporting and extending findings from previous research (Yao et al., 2021; Liu er al., 2022). The basin-wide mode is observed to occur during the summer of the El Niño decaying phase, modulated by PJ teleconnection pattern. This pattern highlights that the mature phase of El Niño in DJF triggers the development of NIO warming and sustains it until JJA, resulting in positive SST anomalies in the NWP via AAC. In contrast, the tripole mode, associated with the El Niño developing summer, emphasizes the role of NPO in shaping the spatial distribution of NWP MHWs. These findings not only corroborate the current understanding of NWP MHW dynamics but also advance our knowledge by clarifying the unique physical mechanisms associated with each mode.

Furthermore, the physics-based empirical prediction models developed in this study, which incorporate preceding anomalous SST and atmospheric circulation indices, exhibit strong predictive skill in forecasting the occurrence and spatial patterns of NWP MHWs several months in advance. The models achieve TCC and RMSE values of 0.65 and 0.77 for PC1, and 0.55 and 0.84 for PC2, respectively, during the period 1982–2022. Both models also well simulate the peak intensity years and the overall spatial distribution of NWP MHWs. Despite these promising results, RMSE values suggest that the physics-based empirical model can be further improved to better capture MHW intensities and finer spatial distribution details. These predictive capabilities are foundational for the development of early warning systems and operational forecasting, which can mitigate the ecological and economic risks associated with NWP MHWs, supporting informed decision-making for coastal communities and fishery management.

Further research is highlighted in several areas. First, this study indicates that the predictability of MHWs is primarily concentrated in the low-latitude NWP, while mid-latitude predictability remains less explored. Previous research has suggested that the zonal-mean component of the summer circumglobal teleconnection pattern is influenced by developing ENSO events (Ding et al., 2011). Identifying and strengthening the link between this teleconnection pattern and mid-latitude NWP MHWs may provide a valuable source of mid-latitude predictability. Additionally, further inclusion of high-resolution regional climate models and ML technology may enhance the precision of the physics-based empirical model, enabling more localized surface and subsurface MHW forecasts with improved lead times. Furthermore, future studies could also explore the physical processes underlying the impact of anthropogenic climate change on the frequency and intensity of NWP MHWs, given the increasing prevalence of extreme MHW events under global warming (Sun et al., 2023; Tang et al., 2023). In particular, greenhouse gas and anthropogenic aerosol forcing may alter the frequency and intensity of ENSO, PJ, and NPO patterns, potentially amplifying or modifying the identified modes. These changes may have significant implications for MHW predictability and the resilience of marine ecosystems in the NWP.

Acknowledgments

We sincerely appreciate the valuable feedback from the three anonymous reviewers, which has greatly improved the quality of this manuscript. This work is jointly sponsored by the National Natural Science Foundation of China (42141019 and 42261144687).

Open Research

All datasets supporting the findings in this study are publicly available. The ERA5 reanalysis data are provided by the Climate Data Store (Hersbach et al., 2023). The HadISST dataset and the monthly EN4 dataset are available from the Met Office Hadley Centre (Rayner et al., 2003; Good et al., 2013). The NOAA OISST v2 High Resolution Dataset is provided by NOAA Physical Sciences Laboratory (Huang et al., 2021). The NCEP–DOE Reanalysis II data and the NCEP GODAS dataset are also available from the Physical Sciences Laboratory (Kanamitsu et al., 2002; Behringer et al., 1998). Global precipitation data are sourced from the Climate Prediction Center (Xie et al., 1997). Monthly chlorophyll-a observations are provided by the NASA Goddard Space Flight Center website (NASA Goddard Space Flight Center, O. B. P. G., 2018).

Conflicts of Interest

The authors declare no competing interests, or other interests that might be perceived to influence the results and/or discussion reported in this study.

References

Behringer, D. W., Ji, M., & Leetmaa, A. (1998). An improved coupled model for ENSO prediction and implications for ocean initialization. Part I: The ocean data assimilation system [Dataset]. Monthly Weather Review, 126(4), 1013-1021. https://doi.org/10.1175/1520-0493(1998)126<1013:AICMFE>2.0.CO;2

Bonino, G., Galimberti, G., Masina, S., McAdam, R., & Clementi, E. (2024). Machine learning methods to predict sea surface temperature and marine heatwave occurrence: a case study of the Mediterranean Sea. Ocean Science, 20(2), 417-432. https://doi.org/10.5194/os-20-417-2024

Chen, Q., Li, D., Feng, J., et al. (2023). Understanding the compound marine heatwave and low-chlorophyll extremes in the western Pacific Ocean. Frontiers in Marine Science, 10, 1303663.

de Burgh-Day CO, Leeuwenburg T. (2023). Machine learning for numerical weather and climate modelling: a review. Geosci Model Dev, 16, 6433–6477. https://doi.org/10.5194/gmd-16-6433-2023

Di Lorenzo, E., Mantua, N. (2016). Multi-year persistence of the 2014/15 North Pacific marine heatwave. Nature Clim Change, 6, 1042–1047. https://doi.org/10.1038/nclimate3082

Ding, Q., Wang, B., Wallace, J. M., & Branstator, G. (2011). Tropical–extratropical teleconnections in boreal summer: Observed interannual variability. Journal of Climate, 24(7), 1878-1896.

Ding, R., Tseng, Y., Di Lorenzo, E. et al. (2022). Multi-year El Niño events tied to the North Pacific Oscillation. Nat Commun, 13, 3871. https://doi.org/10.1038/s41467-022-31516-9

Du, Y., Xie, S. P., Huang, G., and Hu, K. (2009). Role of air–sea interaction in the long persistence of El Niño–induced north Indian Ocean warming. J. Clim, 22(8), 2023–2038. https://journals.ametsoc.org/view/journals/clim/22/8/2008jcli2590.1.xml

Frölicher, T.L., Laufkötter, C. (2018). Emerging risks from marine heat waves. Nat Commun, 9, 650. https://doi.org/10.1038/s41467-018-03163-6

Gao, G., Marin, M., Feng, M., Yin, B., Yang, D., Feng, X., Ding, Y., & Song, D. (2020). Drivers of Marine Heatwaves in the East China Sea and the South Yellow Sea in Three Consecutive Summers During 2016–2018. Journal of Geophysical Research, 125. https://agupubs.onlinelibrary.wiley.com/doi/full/10.1029/2020JC016518

Gill, A. E. (1980). Some simple solutions for heat-induced tropical circulation. Q. J. R. Meteor. Soc, 106(449), 447–462. https://doi.org/10.1002/qj.49710644905

Good, S. A., Martin, M. J., & Rayner, N. A. (2013). EN4: Quality controlled ocean temperature and salinity profiles and monthly objective analyses with uncertainty estimates [Dataset]. Journal of Geophysical Research: Oceans, 118(12), 6704-6716. https://doi.org/10.1002/2013JC009067

Hersbach, H., Bell, B., Berrisford, P., Biavati, G., Horányi, A., Muñoz Sabater, J., Nicolas, J., Peubey, C., Radu, R., Rozum, I., Schepers, D., Simmons, A., Soci, C., Dee, D., Thépaut, J-N. (2023). ERA5 monthly averaged data on single levels from 1940 to present [Dataset]. Copernicus Climate Change Service (C3S) Climate Data Store (CDS), DOI: 10.24381/cds.f17050d7

Hobday, A. J., and Coauthors, 2016: A hierarchical approach to defining marine heatwaves. Prog. Oceanogr., 141, 227-238, https://doi.org/10.1016/j.pocean.

2015.12.014.

Holbrook, N.J., Scannell, H.A., Sen Gupta, A. et al. (2019). A global assessment of marine heatwaves and their drivers. Nat Commun, 10, 2624. https://doi.org/10.1038/s41467-019-10206-z

Hu, S., Zhang, L., & Qian, S. (2020). Marine heatwaves in the Arctic region: Variation in different ice covers. Geophysical Research Letters, 47(16), e2020GL089329. https://doi.org/10.1029/2020GL089329

Huang, B., Liu, C., Banzon, V., Freeman, E., Graham, G., Hankins, B., Smith, T. and Zhang, H.M., 2021. Improvements of the daily optimum interpolation sea surface temperature (DOISST) version 2.1 [Dataset]. Journal of Climate, 34(8), pp.2923-2939. https://doi.org/10.1175/JCLI-D-20-0166.1

Jacox, M.G., Alexander, M.A., Amaya, D. et al. (2022). Global seasonal forecasts of marine heatwaves. Nature, 604, 486–490. https://doi.org/10.1038/s41586-022-04573-9

Kosaka Y., Xie S P., Lau N C. et al. (2013). Origin of seasonal predictability for summer climate over the Northwestern Pacific. Proceedings of the National Academy of Sciences, 110(19), 7574-7579. https://doi.org/10.1073/pnas.1215582110

Li, J., Wang, B. (2016). How predictable is the anomaly pattern of the Indian summer rainfall? Clim Dyn, 46, 2847–2861. https://doi.org/10.1007/s00382-015-2735-6

Liebmann, B., C. A. Smith. (1996). Description of a complete (interpolated) outgoing longwave radiation data set. Bulletin of the American Meteorological Society, 77(6), 1275–1277. https://www.jstor.org/stable/26233278

Liu K, Xu K, Zhu C, et al. (2022). Diversity of Marine Heatwaves in the South China Sea Regulated by ENSO Phase, Journal of Climate, 35(2): 877-893. https://doi.org/10.1175/JCLI-D-21-0309.1

Long, Y., Li, J., Zhu, Z. et al. (2022). Predictability of the anomaly pattern of summer extreme high-temperature days over southern China. Clim Dyn, 59, 1027–1041. https://doi.org/10.1007/s00382-022-06170-y

Lyu, Y., Xiao, F., Lu, M., et al. (2024). Increased frequency but decreased intensity of marine heatwaves around coral reef regions in the Southern South China Sea. Journal of Geophysical Research: Oceans, 129(9), e2024JC021235.

Kanamitsu, M., Ebisuzaki, W., Woollen, J., Yang, S. K., Hnilo, J. J., Fiorino, M., & Potter, G. L. (2002). NCEP–DOE AMIP-II Reanalysis (R-2) [Dataset]. Bulletin of the American Meteorological Society, 83(11), 1631-1643. https://doi.org/10.1175/BAMS-83-11-1631

Ma, et al. (2024). The forecast skills and predictability sources of marine heatwaves in the NUIST-CFS1.0 hindcasts. Advance in Atmospheric Sciences, 41(8), 1589-1600. https://doi.org/10.1007/s00376-023-3139-x

Matsuno, T. (1966). Quasi-geostrophic motions in the equatorial area. Journal of the Meteorological Society of Japan, 44, 25–43. https://doi.org/10.2151/jmsj1965.44.1_25

McPhaden, M. J. (1999). Genesis and evolution of the 1997-98 El Niño. Science, 283(5404), 950-954.

Mills, K. E., et al. (2013). Fisheries management in a changing climate. Oceanography Society, 26(2), 191–195. https://www.jstor.org/stable/24862052

NASA Goddard Space Flight Center, O. B. P. G. (2018). Moderate-resolution Imaging Spectroradiometer (MODIS) Aqua Chlorophyll Data [Dataset]. https://doi.org/10.5067/AQUA/MODIS/L3M/CHL/2018 NASA OB.DAAC, Greenbelt, MD, USA.

Oliver, E., Benthuysen, J., Bindoff, N. et al. (2017). The unprecedented 2015/16 Tasman Sea marine heatwave. Nat Commun, 8, 16101. https://doi.org/10.1038/ncomms16101

Oliver, E. C. J., Burrows, M. T., Donat, M. G., Sen Gupta, A., Alexander, L. V., Perkins-Kirkpatrick, S. E., et al. (2019). Projected marine heatwaves in the 21st century and the potential for ecological impact. Frontiers in Marine Science, 6. https://doi.org/10.3389/fmars.2019.00734

Rayner, N. A., Coauthors. (2003). Global analyses of sea surface temperature, sea ice, and night marine air temperature since the late nineteenth century [Dataset]. Climate and Dynamics, 108, 4407. https://doi.org/10.1029/2002JD002670

Smale, D.A., Wernberg, T., Oliver, E.C.J. et al. (2019). Marine heatwaves threaten global biodiversity and the provision of ecosystem services. Nature Climate Change, 9, 306–312. https://doi.org/10.1038/s41558-019-0412-1

Sun, W., Yin, L., Pei, Y., et al. (2023). Marine heatwaves in the Western North Pacific Region: Historical characteristics and future projections. Deep Sea Research Part I: Oceanographic Research Papers, 200, 104161.

Song, Q., Yao, Y., & Wang, C. (2023). Response of future summer marine heatwaves in the South China Sea to enhanced western Pacific subtropical high. Geophysical Research Letters, 50(14), e2023GL103667. https://doi.org/10.1029/2023GL103667

Tang, H., Wang, J., Chen, Y., et al. (2023). Human contribution to the risk of 2021 Northwestern Pacific concurrent marine and terrestrial summer heat. Bulletin of the American Meteorological Society, 104(3), E673-E679.

Vecchi, G. A., & Harrison, D. E. (2000). Tropical Pacific sea surface temperature anomalies, El Niño, and equatorial westerly wind events. Journal of climate, 13(11), 1814-1830.

Vimont D J., Battisti D S., Hirst A C. (2001). Footprinting: A seasonal connection between the tropics and mid-latitudes. Geophysical Research Letters, 28(20): 3923-3926. https://doi.org/10.1029/2001GL013435

Wang, B. (1992). The vertical structure and development of the ENSO anomaly mode during 1979-1989. Journal of the Atmospheric Sciences, 49(8), 698–712. https://doi.org/10.1175/1520-0469(1992)049<0698:TVSADO>2.0.CO;2

Wernberg, T., Smale, D., Tuya, F. et al. (2013). An extreme climatic event alters marine ecosystem structure in a global biodiversity hotspot. Nature Clim Change, 3, 78–82. https://doi.org/10.1038/nclimate1627

Wu, R., Kirtman, B. P., and Krishnamurthy, V. (2008). An asymmetric mode of tropical Indian Ocean rainfall variability in boreal spring. J. Gophys. Res: Atmospheres, 113(D5). https://doi.org/10.1029/2007JD009316

Xie, P., and P. A. Arkin. (1997). Global precipitation: A 17-year monthly analysis based on Gauge observations, satellite estimates, and numerical model outputs [Dataset]. Bull. Amer. Meteor. Soc, 78, 2539–2558. https://doi.org/10.1175/1520-0477(1997)078<2539:GPAYMA>2.0.CO;2

Xie, S. P., Hu, K., Hafner, J., Tokinaga, H., Du, Y., Huang, G., et al. (2009). Indian Ocean capacitor effect on Indo–western Pacific climate during the summer following El Niño. J. Clim, 22(3), 730–747. https://doi.org/10.1175/2

008JCLI2544.1

Yao, Y., & Wang, C. (2021). Variations in summer marine heatwaves in the South China Sea. Journal of Geophysical Research: Oceans, 126(10), e2021JC017792. https://doi.org/10.1029/2021JC017792

Yao, Y., Wang, C., & Wang, C. (2023). Record-breaking 2020 summer marine heatwaves in the western North Pacific. Deep Sea Research Part II: Topical Studies in Oceanography, 209, 105288.

Yao, M., Li, J., Zheng, C., Yao, M., & Zhu, Z. (2024). How predictable is the anomaly pattern of summer extreme high-temperature days over Central Asia?. Climate Dynamics, 1-14.

Zhang R., Jia X., Qian Q. (2022). Analysis of lower-boundary climate factors contributing to the summer heatwave frequency over eastern Europe using a machine-learning model. Atmospheric Ocean Sci Lett, 15(5), 100256. https://doi.org/10.1016/j.aosl.2022.100256

Zhang, W., Huang, Z., Jiang, F., Stuecker, M. F., Chen, G., and Jin, F. F. (2021). Exceptionally persistent Madden-Julian Oscillation activity contributes to the extreme 2020 East Asian summer monsoon rainfall. Geophysical Research Letters, 48(5), e2020GL091588. https://doi.org/10.1029/2020GL091588

Zhang, T., Xu, H., Ma, J., & Deng, J. (2023). Predictability of Northwest Pacific marine heatwaves in summer based on NUIST-CFS1. 0 hindcasts. Weather and Climate Extremes, 42, 100617. https://doi.org/10.1016/j.wace.2023.100617

Zheng, J., Xiu, P., Zeng, L., Zhu, X., Ji, X., Gao, S., & Li, Z. (2024). Phytoplankton response to the record-breaking marine heatwave in the summer of 2020 in the South China Sea. Journal of Geophysical Research: Oceans, 12

9(10), e2024JC021275.

Table 1. Description of experiments and the corresponding SST boundary conditions in ECHAM6.

Experiment Name	**SST boundary conditions**
Control	Climatological SST and sea ice with seasonal cycle
NIO	1°C warming in the NIO (0°–25°N, 40°E–100°E) is added on the climatological SST
WP	1°C cooling in the WP (5°S–5°N, 160°E–150°W) is added on the climatological SST
NIO–WP	1°C warming in the NIO (0°–25°N, 40°E–100°E) and 1°C cooling in the WP (5°S–5°N, 160°E–150°W) are added on the climatological SST

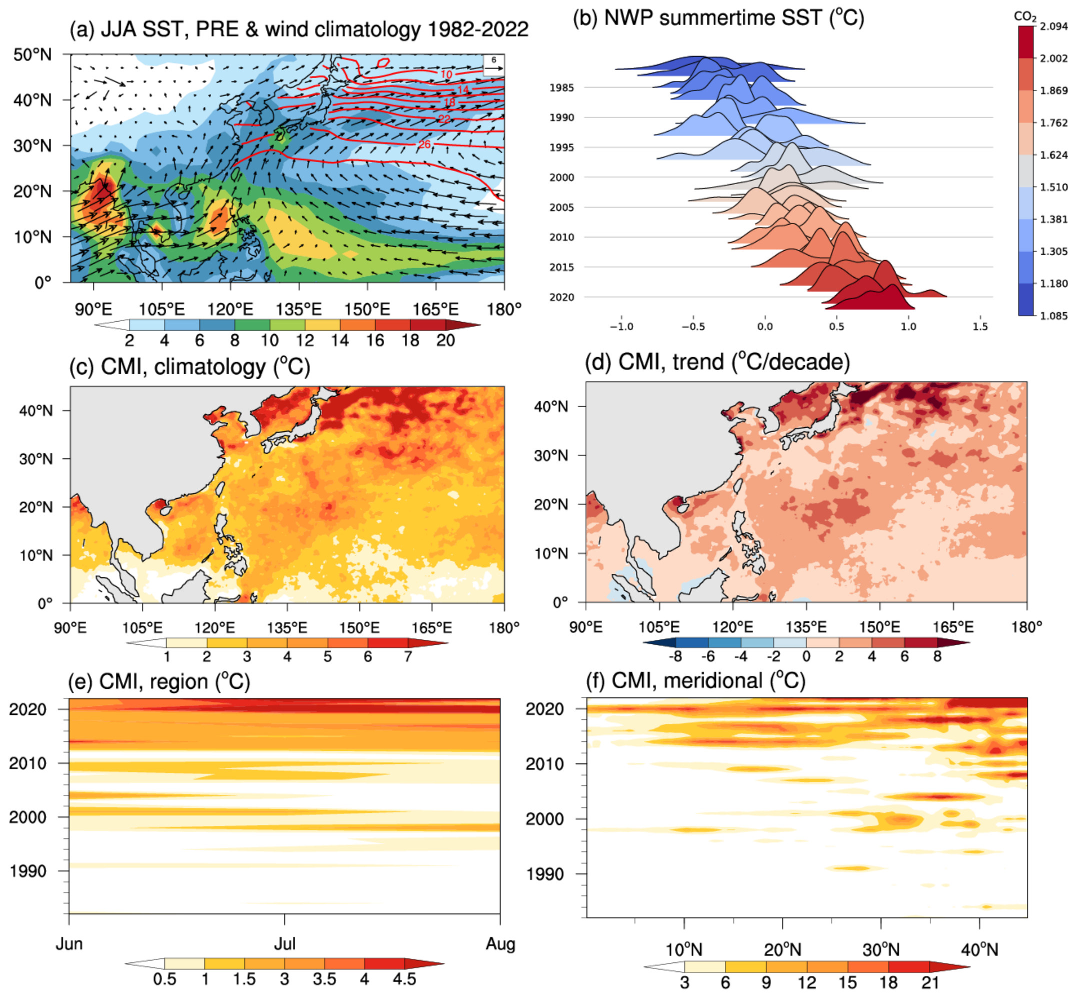

Figure 1. Spatial and temporal distribution of summer MHWs in the NWP during 1982–2022. (a) Climatological distribution of precipitation (shading; mm/day), SST (contour; °C) and 850 hPa winds (vector; $m\ s^{-1}$). (b) Ridgeline plots of summer SST anomaly (probability density curves; °C) under historical CO_2 forcing (shading; W/m²) above 1983–2012 average. (c) Climatological spatial distribution of CMI (°C). (d) Spatial distribution of CMI trend (°C/decade). (e) Sub-seasonal variation of area-weighted regional mean CMI in the NWP. (f) Latitude–time diagram for meridional mean CMI (°C) during 1982–2022.

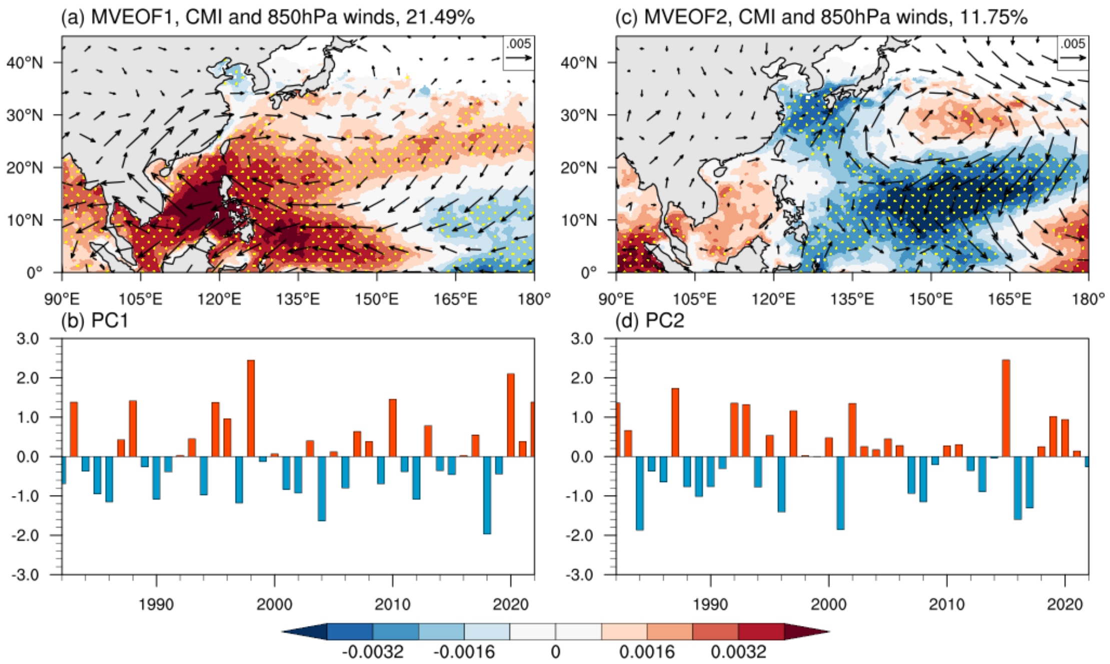

Figure 2. Spatial patterns (a, c) and corresponding PCs (b, d) of the leading two MV-EOF modes of summer MHWs in the NWP during 1982–2022. The first and the second mode explain 21.49% and 11.75% of the total variance, respectively. Stippling indicates values that are above the 90% significance level.

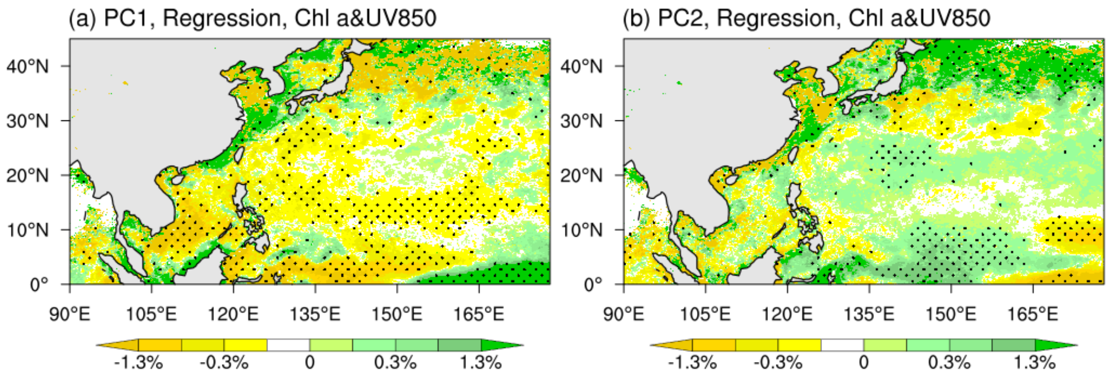

Figure 3. Regression of chlorophyll-a (shading; anomaly percentage) against PC1 (a) and PC2 (b) during 2003–2022. Stippling indicates values that are above the 90% significance level.

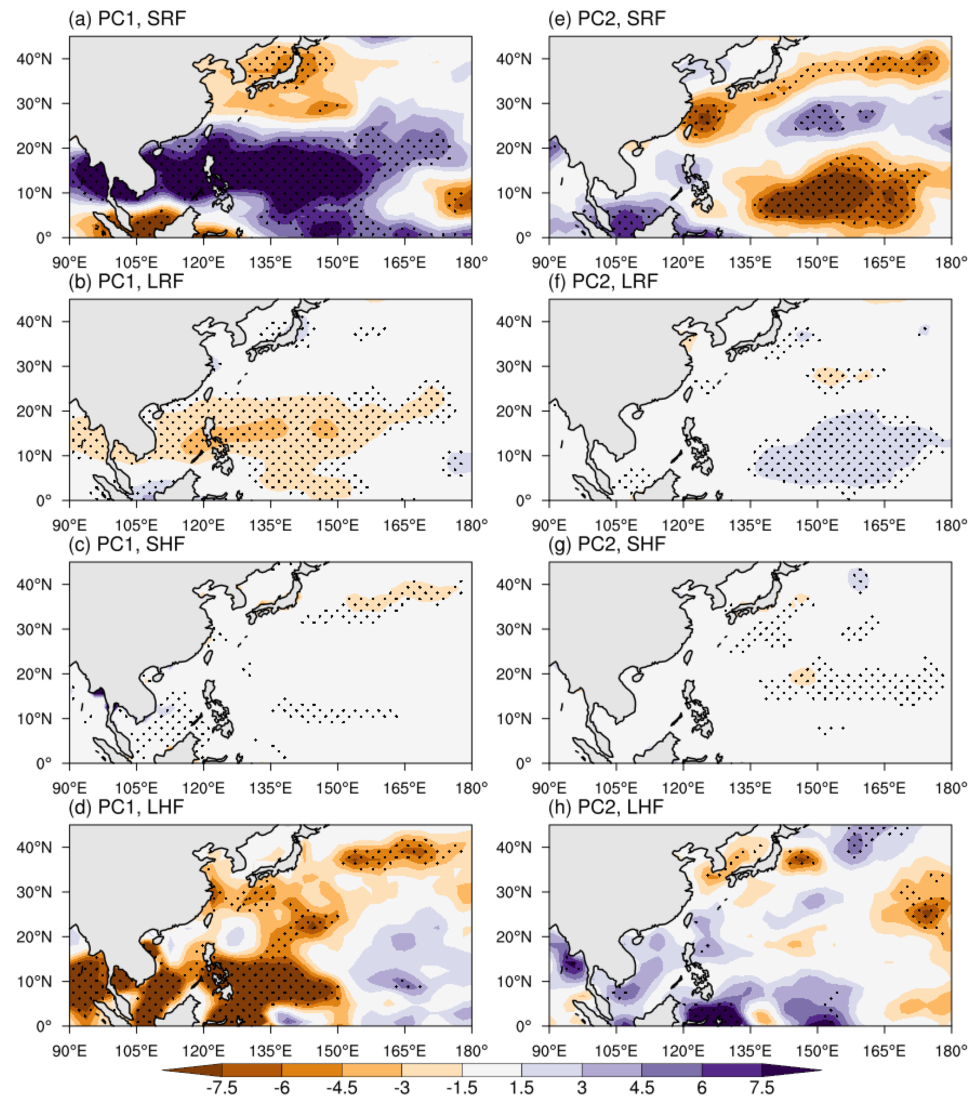

Figure 4. Regression of SRF (downward positive), LRF (downward positive), SHF (upward positive) and LHF (upward positive) (shading; $W\ m^{-2}$) against PC1 (a, b, c, d) and PC2 (e, f, g, h) during 1982–2022. Stippling indicates values that are above the 90% significance level.

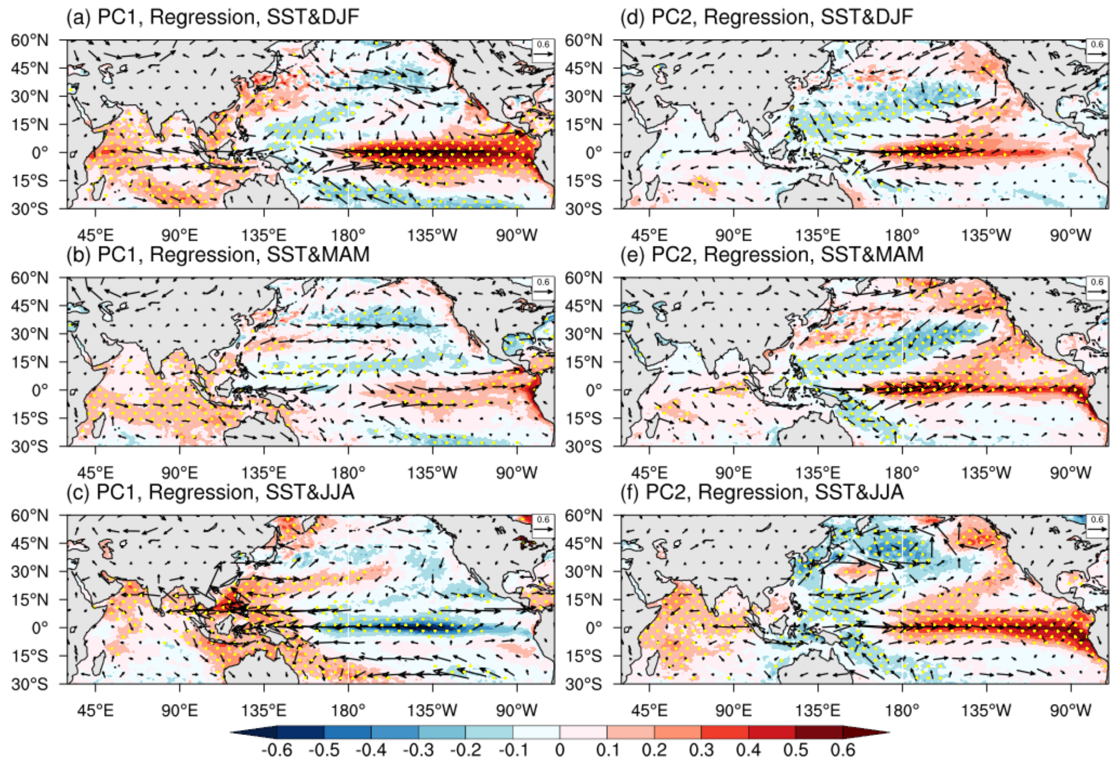

Figure 5. Regression of SST (shading; °C) and 850 hPa wind (vectors; $m\ s^{-1}$) in the preceding DJF (a, d), preceding MAM (b, e) and JJA (c, f) against PC1 (a, b, c) and PC2 (d, e, f) during 1982–2022. Stippling indicates values that are above the 90% significance level.

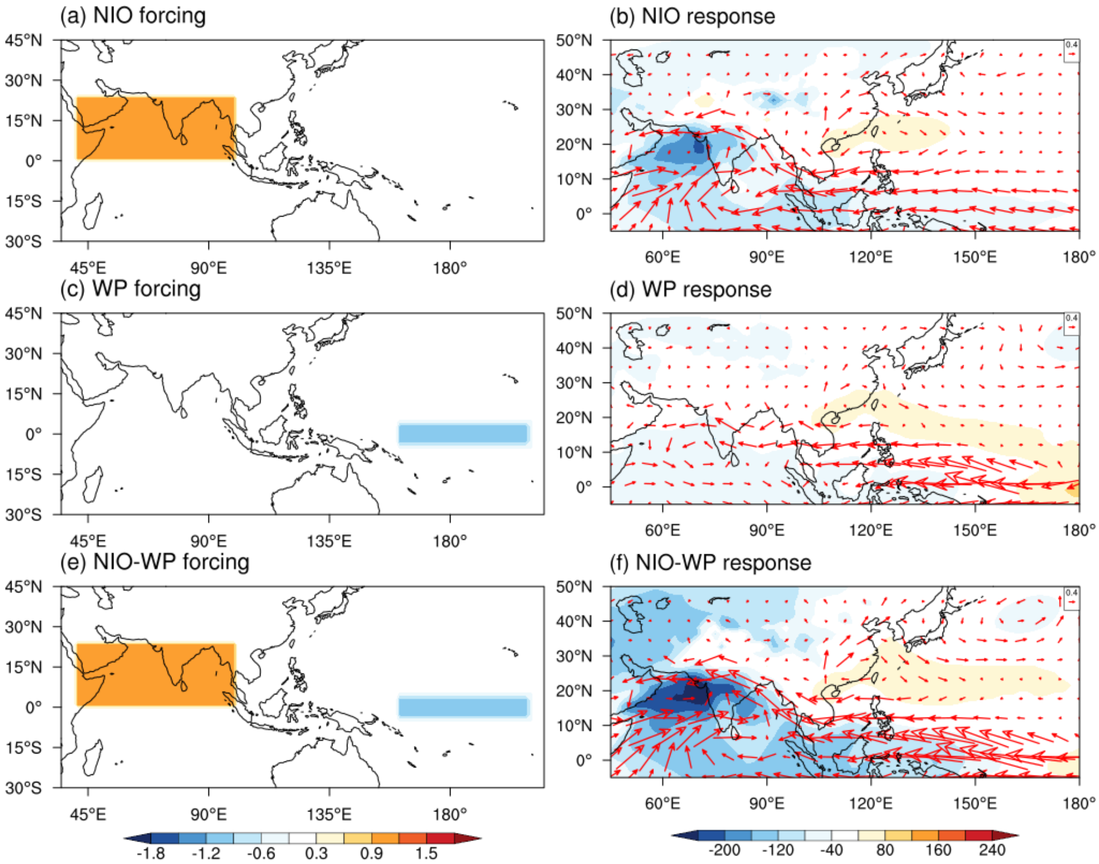

Figure 6. (a) Horizontal distribution of imposed NIO warming. (b) 850-hPa wind (vector) and SLP (shading) response to the imposed NIO warming in ECHAM6. (c–d) Same as (a–b), but for WP cooling. (e–f) Same as (a–b), but for the combination of NIO warming and WP cooling.

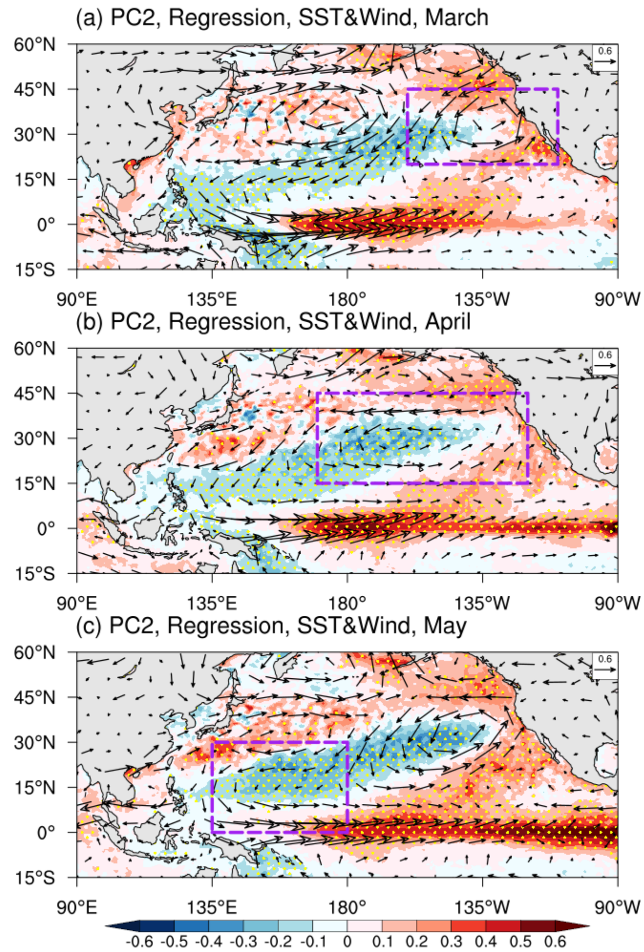

Figure 7. Regression of SST (shading; °C) and 850 hPa wind (vector; $m\ s^{-1}$) in the preceding March (a), preceding April (b), and preceding May (c) against PC2 during 1982–2022. Stippling indicates values that are above the 90% significance level. The purple box denotes the location of the anomalous cyclonic circulation.

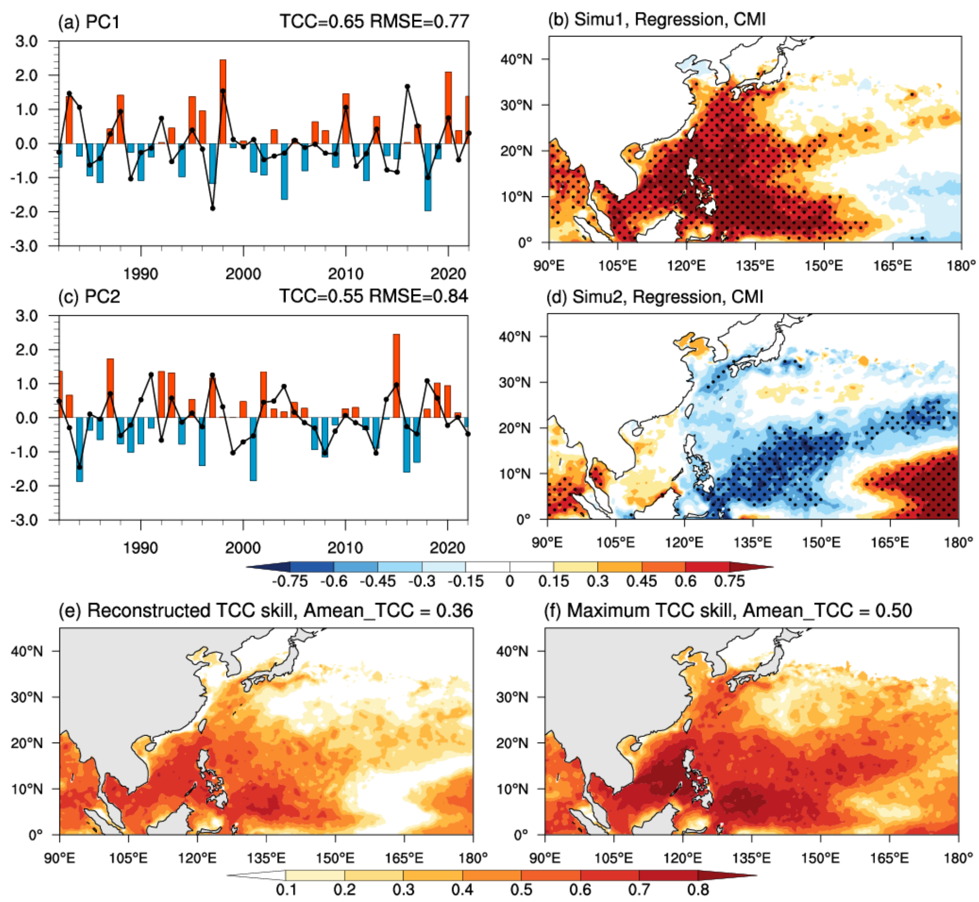

Figure 8. The observed (bars) and independent forecasted (black lines) PC of the first (a) and second (c) MV-EOF mode during 1982–2022. TCC and RMSE skills are shown on the right top of each panel. Regression of summer CMI (shading; °C) against Simu1 (b) and Simu2 (d) (black lines in a and c, respectively). Stippling indicates values that are above the 90% significance level. The distribution of the reconstructed (e) and maximum attainable (f) TCC skills during 1982–2022. The area-weighted regional mean TCC skills over the NWP are shown on the right top of each panel.